Analysis of Multipath Components Distributions Over a Large Array in Indoor mmWave Channels

Alfred Mudonhi, Raffaele D'Errico, *Senior Member, IEEE*, Claude Oestges, *Fellow, IEEE*.

***Abstract*—In this paper, we analyze the characteristics of indoor radio channel at milliliter waves. Measurements were performed using a large virtual antenna array, for massive MIMO (Multiple Input Multiple Output) applications. The results in terms of correlation and multipath components characteristics are analyzed for the whole large array and virtual sub-arrays composing it. Common multipath components among the sub-arrays are identified and the impact on the overall channel large scale parameters, is discussed.**

***Index Terms*—Indoor Propagation, Millimeter waves, Massive MIMO.**

I. INTRODUCTION

MASSIVE Multiple Input Multiple Output (MIMO) technology have been widely investigated in the last years to increase the channel capacity, the wireless link reliability, and to reduce interference [1]. While most of the classical MIMO system implementations employ only a few number of antennas (typically less than ten), the use of extremely large antenna array results into an order of magnitude of more radiating elements. This allows improving the number of data streams, thanks to channel hardening, such that the small-scale fading is mitigated, and reduce the transmitted energy at antenna port, thanks to the large beamforming gain [2].

Massive MIMO benefits have been widely investigated in sub-6 GHz bands, and are considered as fundamental technology for millimiter waves (mmWave) to counteract the large losses at these frequencies.

Nevertheless the implementation of massive MIMO implies a large number of radio frequency chains, hence larger cost and energy consumption, and an important use of resources to determine the channel state information (CSI). These challenges can be solved through hybrid approaches [3].

Obviously, the propagation channel characteristics play a pivotal role in determining the fundamental limits of such communication systems.

Novel ideas such as the deployment of Extremely Large Aperture Arrays for cell-free massive MIMO and holographic massive MIMO among others, imply to solve some new channel modeling related challenges about non-wide-sense stationarity and near field effects [4].

In the past, extensive massive MIMO channel measurements in the sub-6 GHz bands [5], [6], [7], [8] have been carried out and shown the non-stationarity phenomenon over massive arrays at these frequencies. In [9], a channel measurement campaign was conducted at 11 GHz in an indoor lobby environment deploying two different types of 256-element virtual array. In [10], the authors showed that the non-stationarity properties of the massive MIMO channel change several important MIMO design aspects. In essence, for the same number of antenna elements, sub-6GHz massive MIMO arrays are relatively bigger (in size) than the mmWave massive MIMO arrays.

Under these conditions, the plane wave assumption may no longer hold since the curvature of the wave fronts cannot be neglected over large dimensions array. To catch these effects, authors in [11] introduced an intermediate parabolic wave model, which is more accurate than the plane wave model while less complex than the spherical wave model. As for the mmWave massive MIMO, the very high frequencies correspond to smaller wavelengths and as a result, smaller arrays. Despite the compact arrays, the far field assumption may still be breached in the short-range mmWave communications.

The extensive measurements and simulations carried out in [12] showed that circularly polarized (CP) antennas achieve better performance and reliability over linearly polarized (LP) ones in indoor environments (considering only the direct ray or the multipath propagation). Additional studies and extensive investigations employing either CP or LP antennas in the context of mmWave massive MIMO still need to be done.

In the last years, the scientific community have been proposing different channel models for 5G communications, including world-wide recognized standards from ITU and 3GPP [13] and first approaches to 3-D wideband model for 5G massive MIMO channels [14], [15], [16]. However mmWave channel modeling is often based on mechanical steering of antennas and reconstruction of the omni-directional power angular delay profile, while the properties of massive MIMO mmWave channel for short ranges, typically in indoor environments, demand for specific measurement campaigns and analysis. In this paper, we tackle the problem of mmWave massive MIMO channel characterization in indoor premises. In particular, we analyze how in Line-of-Sight (LOS) condition, the channel variates along a large array of 21×21 antennas. In view of hybrid beamforming approaches, where different sub-arrays could be exploited, we analyze the multipath components (MPCs) distributions and similarities between different

Submitted June 3,2021. "This work was partially funded by the ANR project MESANGES, and H2020 project RISE-6G. "

The authors are thankful to Dr. Gloria Makhoul for the fruitful discussion and contribution to SAGE algorithm.

A. Mudonhi was with CEA-Leti, 17 Avenue des Martyrs, 38054 Grenoble, France, and the Université Grenoble-Alpes, 621 avenue Centrale, 38400 Saint Martin d'Hères, France and ICTEAM Université catholique de Louvain, Place du Levant 3/L5.03.02, 1348 Louvain-la-Neuve, Belgium.

R. D'Errico is with CEA-Leti, 17 Avenue des Martyrs, 38054 Grenoble, France. (e-mail: raffaele.derrico@cea.fr).

C. Oestges is with ICTEAM Université catholique de Louvain, 1348, Louvain-la-Neuve, Belgium. (e-mail: claude.oestges@uclouvain.be).

positions within the large array. The paper is structured as follows: in Section II, the measurement campaign in the 26-30 GHz band is presented; section III discusses the spatial channel correlation over the large array; section IV outlines the methodology for common path identification among different sub-arrays, along with the results in Section V. Finally Section VI concludes the paper.

II. Measurement Campaign

The channel measurements are performed in a laboratory room, as illustrated in Fig. 1(a). The dimensions of the room

(a) Environment

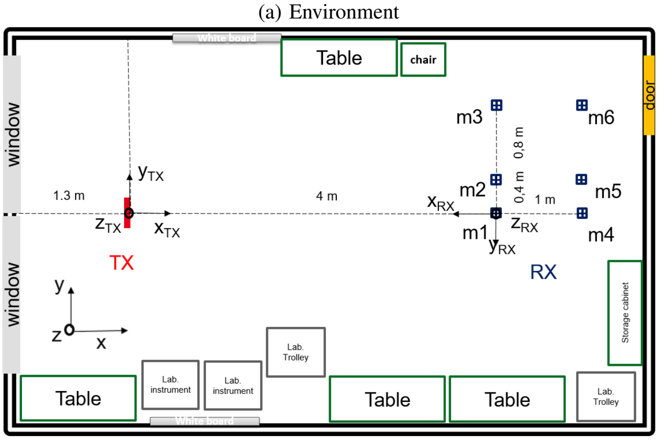

(b) Floor plans

Fig. 1: The measurement environment and the floor plans.

are 7 m × 4.3 m × 2.8 m. The measurement setup is based on a 4-port Vector Network Analyzer (VNA) and two automatic positioners to control antenna movements while scanning virtual spatial grids. The instruments are controlled by an external PC. Two identical vertically polarized monopole antennas of gain 1 dBi were employed at a height of 1.54 m above the ground. Measurements were performed in the frequency band 26-30 GHz, sweeping 801 frequency points. The transmitted power was 10 dBm. On the transmit (TX) side, spatial grids were implemented in the z and y axes, forming a 21×21 virtual antenna array (VAA) in the zoy plane. On the receive (RX) side, 3×3 spatial grids are implemented along the x and y axes. With 28 GHz as the centre frequency, a grid step of 5 mm corresponding to half-wavelength was considered on both TX and RX grids. The floor plans, showing the fixed TX position and different RX positions are shown in Fig. 1(b).

III. Channel Correlation over Large Array

Starting from measurement results, we investigate the channel correlation in frequency and delay domains over the large array employed on the transmitting side. For this purpose, the 21 × 21 large array was divided into 49 adjacent sub-arrays of 3 × 3 dimensions as shown in Fig. 1(a). The main purpose is to investigate how different sub-arrays belonging to a large one are correlated. We computed the average maximum correlation amplitude, in the frequency domain, as :

$$\overline{\rho_{f,p,q}} = \mathbb{E}\left[\max_{\Delta f}\left|\frac{\mathbf{H}_{p,i}(f)\cdot\mathbf{H}_{q,i}(f+\Delta f)^{*}}{\sqrt{\mathbf{H}_{p,i}(f)\cdot\mathbf{H}_{p,i}(f)^{*}}\sqrt{\mathbf{H}_{q,i}(f)\cdot\mathbf{H}_{q,i}(f)^{*}}}\right|\right] \quad (1)$$

where $\mathbf{H}_{p,i}(f)$ is channel transfer function related to the p-th sub-array and i-th MIMO link, and $(\cdot)^{*}$ denote the Hermitian transpose operator. In the following results we show the correlation between the central sub-array and the others over the large one. We can notice in Fig.2 that the correlation is generally below 0.6, and for highly correlated sub-arrays, we do not notice a symmetrical behaviour over the large surface. This would suggest a non-stationarity of the channel.

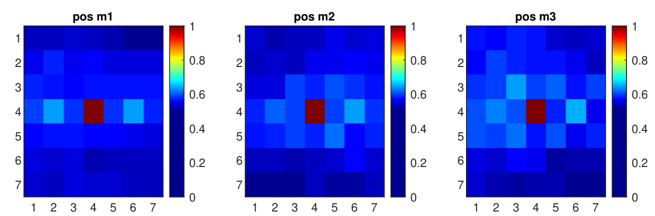

(a) (b) (c)

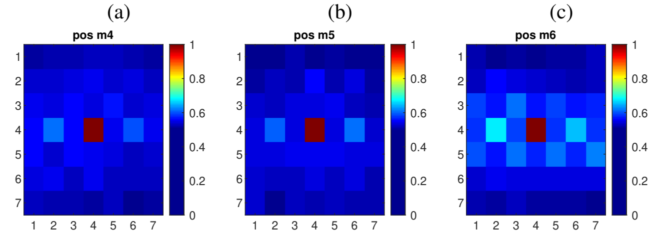

(d) (e) (f)

Fig. 2: $\overline{\rho_{f,p,q}}$: Central sub-array vs 48 other sub-arrays including its autocorrelation at each receiver position.

To further analyze this behaviour, we computed the correlation between different sub-arrays in the delay domain :

$$\overline{\rho_{\tau,p,q}} = \mathbb{E}\left[\max_{\Delta\tau}\frac{\mathbf{P}_{p,i}(\tau)\cdot\mathbf{P}_{q,i}(\tau+\Delta\tau)^{T}}{\sqrt{\mathbf{P}_{p,i}(\tau)\cdot\mathbf{P}_{p,i}(\tau)^{T}}\sqrt{\mathbf{P}_{q,i}(\tau)\cdot\mathbf{P}_{q,i}(\tau)^{T}}}\right] \quad (2)$$

where $\mathbf{P}_{p,i}(\tau)$ is the Power Delay Profile related to the p-th sub-array and i-th MIMO link, and $(\cdot)^{T}$ denote the transpose operator. $\mathbf{P}_{p,i}(\tau)$ is obtained from the measured channel transfer function following (3).

$$\mathbf{P}_{p,i}(\tau) = |\mathbf{h}_{p,i}(\tau)|^{2} = \mathscr{F}^{-1}(\mathbf{H}_{p,i}(f)) \quad (3)$$

where $\mathbf{h}_{p,i}(\tau)$ is the channel impulse response vector and $\mathscr{F}^{-1}$ denote the inverse Fourier Transform.

Two different cases were considered here. In the first case, $\overline{\rho_{\tau,p,q}}$ values were computed including the LOS component using (2). Fig.3 shows $\overline{\rho_{\tau,p,q}}$ when the central sub-array $\mathbf{P}_{p,i}(\tau)$ is cross-correlated with the other sub-arrays PDPs.

It was observed that in considering the LOS component, the minimum $\overline{\rho_{\tau,p,q}}$ for the six receiver positions ranged from 0.66 to 0.84. Given the short distances traversed by the sub-arrays (of about 10 cm), the channel correlation coefficients obtained are consistent with the findings in [17]. In the second case, the cross-correlations were computed excluding the line of sight component (NLOS scenario), and we denote the normalized cross-correlation values as $\overline{\rho_{\tau,p,q}^{NLOS}}$.

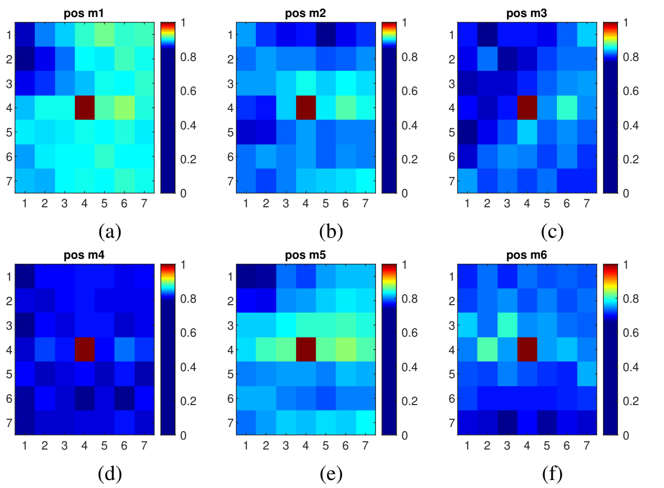

Fig. 3: $\overline{\rho_{\tau,p,q}}$: Central sub-array vs 48 other sub-arrays including its auto-correlation at each receiver position.

Likewise, Fig.4 shows the $\overline{\rho_{\tau,p,q}^{NLOS}}$ for the 6 receiver positions. The minimum $\overline{\rho_{\tau,p,q}^{NLOS}}$ values for the six receiver positions ranged from 0.54 to 0.65.

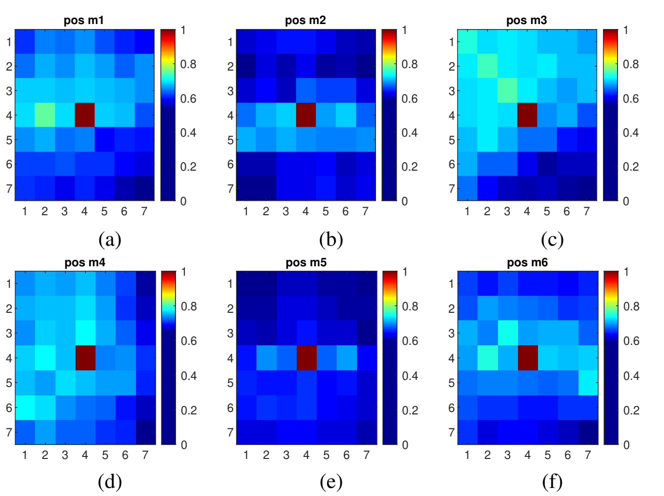

Fig. 4: $\overline{\rho_{\tau,p,q}^{NLOS}}$: Central sub-array vs 48 other sub-arrays including its auto-correlation at each receiver position.

Generally, we observed that the LOS component appears to contribute more to the correlation coefficients of the receivers who are closer to the transmitter e.g (m1 and m2) than it does to the correlation coefficients of the receivers further from the transmitter (m4, m5 and m6). The strong correlation values for position m3, even without the LOS component can be partly explained by the closeness of this position to the walls. Consequently, strong reflections from the walls lead to relatively high correlation values in the delay domain for some sub-arrays as can been in Fig.4(c). In some instances, particularly position m5, excluding the LOS component resulted in a significant decrease in the correlation values, highlighting the dominance of the LOS component at this particular position.

To get further insights, the next steps considered were to extract the MPCs of each of the 49 sub-arrays at a particular position, identify the common paths among the sub-arrays following a joint temporal, power and angular thresholds criterion, and then analyze the MPCs distributions.

IV. Multipath Components Analysis

For the MPCs detection and channel parameters estimations, the UWB-SAGE (Ultra-wideband Space-Alternating Generalized Expectation-Maximization) algorithm was used [18]. MPCs of significant powers were considered in this work (10dB above the noise floor). The maximum number of resolvable MPCs to be estimated was set to 100. The stopping criteria was when more than 95 percent of the measured channel power had been estimated, or otherwise, when the maximum number of the resolvable MPCs had been reached. With our focus placed on the 6 different receiver positions, we identify the common MPCs seen by the 49 sub-arrays at one particular receiver position. Let us define the l-th MPC of the p-th sub-array at a particular receiver position as follows (4):

$$\mathbf{MPC}_l^p = [\alpha_l^p, \tau_l^p, \phi_l^p]^T \tag{4}$$

where α_l^p, τ_l^p, ϕ_l^p are respectively, the amplitude, the delay and the azimuth angle of arrival (AOA) of the l-th MPC of the p-th sub-array. Therefore in our case, we have $p = 1, ..., P$ with $P = 49$, and $l = 1, ..., \mathrm{L}^p$ where L^p is the number of MPCs detected by considering the p-th sub-array. Hence the MPCs detected by the p-th sub-array are given by $\mathbf{MPC}^p = [\mathbf{MPC}_1^p, \mathbf{MPC}_2^p, ..., \mathbf{MPC}_{L^p}^p]$. In order for the detected MPCs between the p-th and the q-th sub-arrays to be considered common, equation (5), given below, has to be met jointly and simultaneously:

$$|\tau_l^p - \tau_l^q| < \Delta\tau \cap \big| |\phi_l^p| - |\phi_l^q| \big| \leq \Delta\phi \cap \big| |(\alpha_l^p)^2| - |(\alpha_l^q)^2| \big| < \Delta\xi \tag{5}$$

where $\Delta\tau$, $\Delta\phi$ and $\Delta\xi$ are the delay threshold in [ns], AoA threshold in [°] and power threshold in [dB], respectively. Effectively, after the common paths identification, the p-th sub-array satisfies the following equation (6):

$$\sum_{l=1}^{L^p} \alpha_l \delta(\tau - \tau_l) \delta(\phi - \phi_l) = \sum_{l=1}^{L^c} \alpha_l \delta(\tau - \tau_l) \delta(\phi - \phi_l) + \sum_{l=L^c+1}^{L^p} \alpha_l \delta(\tau - \tau_l) \delta(\phi - \phi_l) \tag{6}$$

where L^p is the total number of MPCs at the p-th sub-array, L^c is the number of common paths found.

Basically, equation (5) is applied in such a way that each l-th MPC of the p-th sub-array is compared with all the L^q

MPCs of the q-th sub-array (one at a time). In our work, for the delay threshold, we considered any two MPCs to be similar, if the absolute difference of the arrival delays is within 2 ns. This delay threshold accounts for the 1 ns delay bin width considered in the UWB SAGE algorithm as well as twice the 0.5 ns accounting for the furthest distance between two sub-arrays on the extremities of the massive array. Applying physical geometry to positions m1 and m4 for instance, ideally, two MPCs can be considered to be the same if the difference between their azimuth AOAs is about $\Delta\phi \simeq 2°$. It has been seen in this work that applying this strict value results in some MPCs that via visual inspection are similar, being considered different. As a result, tuning of this parameter to $\Delta\phi$ =5° provides consistent results. It is important to remark that AOAs in our work were defined from -180° to 180° and in using (5), an extra step is needed to make sure that in the event of oppositely signed AOAs, only two MPCs whose AOAs are closer to 180 ° or to 0° could be considered common. Fig 5 and Fig 6 serve as examples of the detected common MPCs between two different sub-arrays.

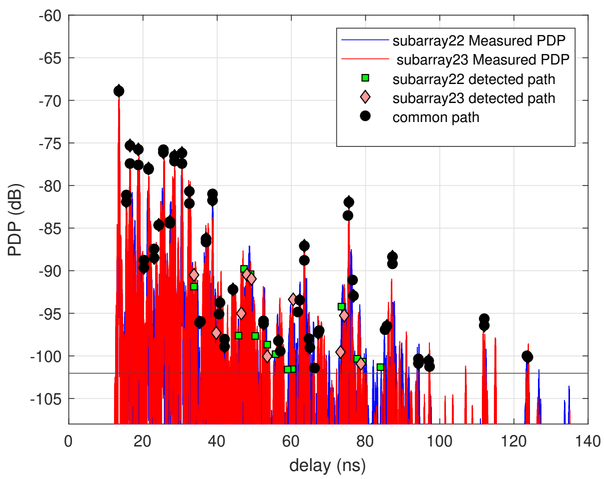

Fig. 5: Position m1 superposed sub-array22 and the reference sub-array23 measured PDPs and the detected and common MPCs.

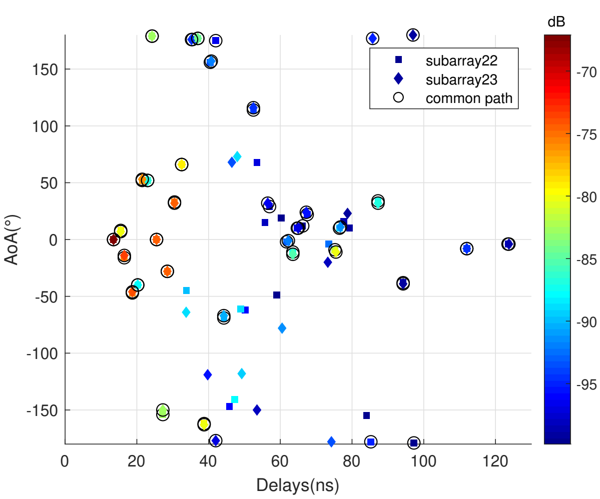

Fig. 6: Position m1 scatter plots of sub-array22 and the reference sub-array23 showing the detected and common MPCs.

As for the MPCs powers, a difference of less than 3 dB between the two MPCs was considered permissible in order for the two MPCs to be deemed similar (common). The results showed that for example, the fourth MPC in one sub-array can be the fifth MPC in the other sub-array and so on.

V. Results

When a massive 21×21 array was compared with the central 3×3 sub-array, it was observed that the LOS path remains the same despite the size of the array and this also holds true for the 49 sub-arrays at one particular receiver position. On the contrary, the size of the array has an impact on the secondary MPCs estimation [19]. The 49 sub-arrays of the massive array, do not see the same channel (shown by the superposed PDP plots of any two sub-arrays). The least and the highest LOS component energy contributions among all 49 sub-arrays at all six receiver positions were 26 % and 49%, respectively. Taking Fig. 7 as an example, the cdf curve (solid line) for position m1 is obtained as follows: for each of the 49 sub-arrays at position m1, a single value of the root mean square delay spread (DS) is computed and this means that eventually we will have 49 DS values and these are the values used to generate the cdf curve of position m1. The same principle is used for the other positions and the DS values for the p-th sub-array are computed using (7):

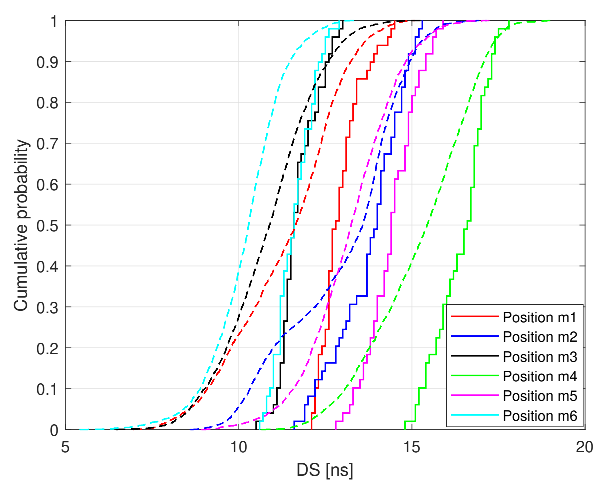

Fig. 7: DS all MPCs and common MPCs. Solid lines show all the MPCs statistics and the dotted lines show the common paths statistics.

$$DS^p = \sqrt{\frac{\sum_{l=1}^{L^p} (\tau_l^p - \tau_m^p)^2 \, (\alpha_l^p)^2}{\sum_{l=1}^{L^p} (\alpha_l^p)^2}} \quad (7)$$

where τ_m^p is the mean arrival delay of the multipaths and is computed as follows:

$$\tau_m^p = \frac{\sum_{l=1}^{L^p} (\alpha_l^p)^2 \tau_l^p}{\sum_{l=1}^{L^p} (\alpha_l^p)^2} \quad (8)$$

L^p, $(\alpha_l^p)^2$ and τ_l^p are the number of detected MPCs, the power of the l-th path and the arrival delay of the l-th path, respectively, for the p-th sub-array. From Fig. 7, the difference between the common paths median DS and all paths median DS value ranges from 0.42 ns to 1.32 ns for all six positions.

With regards to the number of paths shown on Fig. 8, the median number of common paths as a percentage of the median number of all the paths detected was within the range 46.9% to 59.2 % .

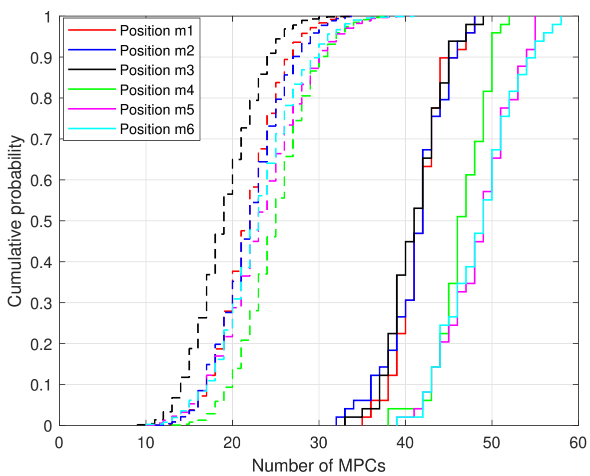

Fig. 8: Number of paths all MPCs and common MPCs. Solid lines show all the MPCs statistics and the dotted lines show the common paths statistics.

The angular spread (AS) values for the p-th sub-array, from which Fig. 9 is derived, are computed using (9):

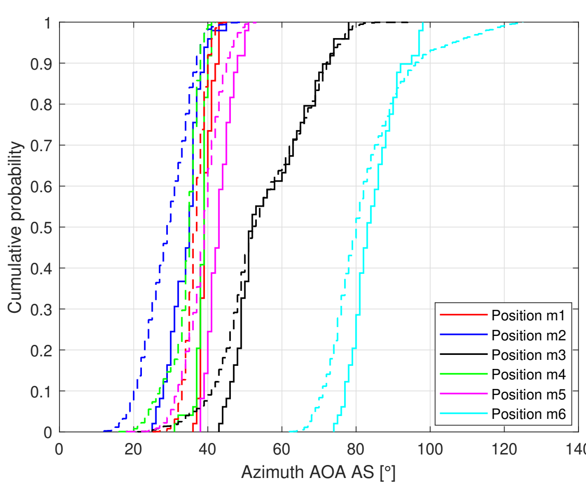

Fig. 9: Azimuth AOA AS all MPCs and common MPCs. Solid lines show all the MPCs statistics and the dotted lines show the common paths statistics.

$$AS^p = \sqrt{-2\ln\left(\left|\frac{\sum_{l=1}^{L^p}\exp\left(j\phi_l^p\right)(\alpha_l^p)^2}{\sum_{l=1}^{L^p}(\alpha_l^p)^2}\right|\right)} \quad (9)$$

where ϕ_l^p is the azimuth angle of arrival (or departure) of the l-th path at the p-th sub-array. The difference between the common paths median azimuth angle of arrival (Azimuth AOA) AS and all paths median Azimuth AOA AS value ranges from 2° to 6° for all the six receiver positions.

Respecting (5), consider for example one particular receiver position (position m1). Each of the 49 sub-arrays is compared with the other sub-arrays (including self-comparison) in order to identify common paths. We call the sub-array that is being compared to the other sub-arrays the reference sub-array. This means that a total of 2401 comparisons are done for the position m1 (each of the 49 sub-arrays having been considered as a reference sub-array). This means that for each p-th reference sub-array, 49 sets of common paths will be identified. Each set, contains the common MPCs identified between the reference sub-array and the other sub-array. For each set of common paths, we then compute the DS, the AS, using (7) and (9), replacing the superscript p with pc=1,...,49 where pc is the pc-th set of common paths obtained in considering the p-th reference sub-array. The energy contributions of these common MPCs (η) with respect to the reference sub-array, are also obtained following (10).

$$\eta^p(\%) = \frac{\sum_{l=1}^{L^c}(\alpha_l^{pc})^2}{\sum_{l=1}^{L^p}(\alpha_l^p)^2} \times 100 \quad (10)$$

where $(\alpha_l^{pc})^2$ is the l-th common MPC power, and $(\alpha_l^p)^2$ is the power of the l-th MPC of the p-th sub-array and pc=1,...,49 where pc is the pc-th set of common paths obtained considering the p-th sub-array as the reference sub-array. We then proceed to generate the cdf of the 2401 sets at position m1 (e.g the red curve in Fig. 10 shows the common MPCs energy contributions). Excluding the reference sub-array's self-comparison results, the minimum common MPCs energy contribution is 43.4% while the maximum contribution is 99.4% for all the six receiver positions. Likewise, the minimum average common paths energy contribution was found to be 76.2% while the maximum average common paths contribution was 87.1%.

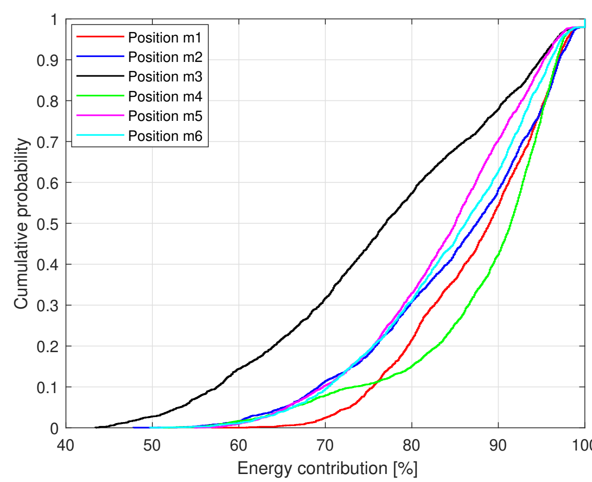

Fig. 10: Common MPCs energy contributions.

In a nutshell, the common MPCs distributions are shown in figures (dotted lines): Fig. 8, Fig. 7 as well as Fig. 9. The common MPCs energy contributions are shown in Fig. 10. We can see that the the common MPCs (which are numerically, 47% to 59% of L^p) have on average, an energy contribution higher (by a factor >2) than the energy contributions of the uncommon paths. Also, the common MPCs, are less spread both in the azimuth and in the elevation than the uncommon MPCs and they have shorter DS compared to the uncommon paths.

Having identified the common MPCs and the uncommon MPCs large scale parameters and their respective energy contributions at each particular receiver position, we will now look at the overall statistics. In essence, all the 6 receiver positions parameters (DS and AS) are combined into a single set of data. Table I shows the minimum, maximum and median values of the aforementioned parameters when different array sizes are considered.

TABLE I: Overall DS and AS statistics considering different TX array sizes .

Parameter	3×3 central sub-array	7×7 sub-array	21×21 massive array	49 (3×3) sub-arrays
Min DS [ns]	11.3	10.4	10.4	10.5
Max DS [ns]	17	16.9	15.6	17.8
Med DS [ns]	13.7	13.6	13	13.1
Min AOA AS [°]	30	29	34	25
Max AOA AS [°]	81	82	87	98
Med AOA AS [°]	41	39	42	41

Fig. 11 shows the variation of the common paths number with distance over the array. The displacements were considered horizontally, vertically and diagonally. The minimum vertical or horizontal displacement distance is 15 mm ($\frac{3\lambda}{2}$) while the maximum vertical or horizontal displacement distance is 90 mm ($\frac{18\lambda}{2}$). Diagonally, the minimum displacement is 21.2 mm and the maximum displacement is 127.3 mm. We can clearly see from Fig.11 that the number of common paths decreases with increase in distance.

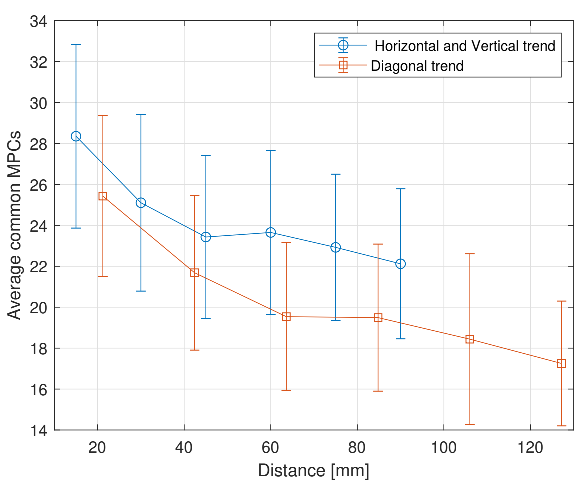

Fig. 11: Overall average common path variation per distance over the massive array

Numerically, the comparison between the overall statistics before the common path identification and the overall statistics of the identified common paths in the investigated indoor laboratory shows that the common path DS and AS are smaller (on average by 1.2 ns and 3°, respectively).

VI. Conclusion

In this work, we have analyzed the MPCs distributions over a massive array in an indoor environment exploiting the mmWave frequency band. The spatial channel correlation was investigated in both the frequency domain and the delay domain (both LOS and NLOS). In both domains (with the delay domain clearly highlighting this), the normalized cross-correlation values do not have a symmetric behaviour over the large array, suggesting non-stationarity over the large array. The multipath components were extracted for the whole large array and sub-arrays defined within, using SAGE algorithm. A joint temporal, power and angular thresholds criterion was employed to identify common MPCs among different sub-arrays. The results show that these common paths have a an important energy contribution in the Line of Sight scenarios considered. However, in order to fully catch the channel characteristics, the sub-array dependent paths, here called uncommon, should also be considered. The impact of these components was investigated for different sub-array sizes, showing that their contribution can reach up to 56.6% of the energy even in Line of Sight. A model based on only common multipaths could yield to an underestimation of angular and delay spread. The shorter delay spreads and smaller angular spreads for the common multipath components may suggest that efficient mmWave massive MIMO systems exploiting hybrid beamforming based on sub-array division can be achieved. On the one hand, shorter delay spreads imply flat fading, which has an impact on wideband orthogonal frequency-division multiplexing (OFDM) systems, where analog beamformers can hardly have different weights across subcarriers. On the other hand, by taking advantage of a small angular spread at the base station sub-array, we can reduce the dimension of the effective instantaneous channel state information for digital beamforming within each coherent fading block. However, as already highlighted above, at some receiver positions, the uncommon paths energy contribution can be significant, therefore caution needs to be applied when designing such mmWave massive MIMO systems employing sub-array based beamforming. Hence, these effects need to be carefully taken into account for mmWave massive MIMO channel characterization for indoor applications.

References

[1] T. L. Marzetta, “Noncooperative Cellular Wireless with Unlimited Numbers of Base Station Antennas,” *IEEE Transactions on Wireless Communications*, vol. 9, no. 11, pp. 3590–3600, 2010.

[2] E. Björnson, J. Hoydis, and L. Sanguinetti, "Massive MIMO Networks: Spectral, Energy, and Hardware Efficiency," *Foundations and Trends® in Signal Processing*, vol. 11, no. 3-4, pp. 154–655, 2017.
[3] A. F. Molisch, V. V. Ratnam, S. Han, Z. Li, S. L. H. Nguyen, L. Li, and K. Haneda, "Hybrid Beamforming for Massive MIMO: A Survey," *IEEE Communications Magazine*, vol. 55, no. 9, pp. 134–141, 2017.
[4] E. Björnson, L. Sanguinetti, H. Wymeersch, J. Hoydis, and T. L. Marzetta, "Massive MIMO is a reality—What is next?: Five Promising Research Directions for Antenna Arrays," *Digital Signal Processing*, vol. 94, pp. 3–20, 2019.
[5] X. Gao, O. Edfors, F. Tufvesson, and E. G. Larsson, "Massive MIMO in Real Propagation Environments: Do All Antennas Contribute Equally?" *IEEE Transactions on Communications*, vol. 63, no. 11, pp. 3917–3928, 2015.
[6] S. Payami and F. Tufvesson, "Channel Measurements and Analysis for Very Large Array Systems at 2.6 GHz," in *2012 6th European Conference on Antennas and Propagation (EUCAP)*. IEEE, 2012, pp. 433–437.
[7] X. Gao, F. Tufvesson, O. Edfors, and F. Rusek, "Measured propagation characteristics for very-large MIMO at 2.6 GHz," in *2012 Conference Record of the Forty Sixth Asilomar Conference on Signals, Systems and Computers (ASILOMAR)*. IEEE, 2012, pp. 295–299.
[8] J. Hoydis, C. Hoek, T. Wild, and S. ten Brink, "Channel Measurements for Large Antenna Arrays," in *2012 International Symposium on Wireless Communication Systems (ISWCS)*. IEEE, 2012, pp. 811–815.
[9] J. Li, B. Ai, R. He, M. Yang, Z. Zhong, Y. Hao, and G. Shi, "The 3D Spatial Non-Stationarity and Spherical Wavefront in Massive MIMO Channel Measurement," in *2018 10th International Conference on Wireless Communications and Signal Processing (WCSP)*. IEEE, 2018, pp. 1–6.
[10] E. De Carvalho, A. Ali, A. Amiri, M. Angjelichinoski, and R. W. Heath, "Non-Stationarities in Extra-Large-Scale Massive MIMO," *IEEE Wireless Communications*, vol. 27, no. 4, pp. 74–80, 2020.
[11] L. Le Magoarou, A. Le Calvez, and S. Paquelet, "Massive MIMO Channel Estimation taking into account spherical waves," in *2019 IEEE 20th International Workshop on Signal Processing Advances in Wireless Communications (SPAWC)*. IEEE, 2019, pp. 1–5.
[12] F. A. Dicandia, S. Genovesi, and A. Monorchio, "Analysis of the performance enhancement of MIMO systems employing circular polarization," *IEEE Transactions on Antennas and Propagation*, vol. 65, no. 9, pp. 4824–4835, 2017.
[13] 3GPP TR 38.901, "5G; Study on channel model for frequencies from 0.5 to 100 GHz ," Tech. Rep., version 16.1.0, Release 16, 2020.
[14] S. Wu, C.-X. Wang, M. M. Alwakeel, Y. He *et al.*, "A Non-Stationary 3-D Wideband Twin-Cluster Model for 5G Massive MIMO Channels," *IEEE journal on selected areas in communications*, vol. 32, no. 6, pp. 1207–1218, 2014.
[15] Y. Xie, B. Li, X. Zuo, M. Yang, and Z. Yan, "A 3D Geometry-based Stochastic Model for 5G Massive MIMO Channels," in *2015 11th International Conference on Heterogeneous Networking for Quality, Reliability, Security and Robustness (QSHINE)*. IEEE, 2015, pp. 216–222.
[16] K. Zheng, S. Ou, and X. Yin, "Massive MIMO Channel Models: A Survey," *International Journal of Antennas and Propagation*, vol. 2014, 2014.
[17] Y. Tan, J. Ø. Nielsen, and G. F. Pedersen, "Spatial Stationarity of Ultrawideband and Millimeter Wave Radio Channels," *International Journal of Antennas and Propagation*, vol. 2016, 2016.
[18] K. Haneda and J.-I. Takada, "An application of SAGE algorithm for UWB propagation channel estimation," in *IEEE Conference on Ultra Wideband Systems and Technologies, 2003*. IEEE, 2003, pp. 483–487.
[19] A. Mudonhi, R. D'Errico, and C. Oestges, "Indoor mmWave Channel Characterization with Large Virtual Antenna Arrays," in *2020 14th European Conference on Antennas and Propagation (EuCAP)*. IEEE, 2020, pp. 1–5.

Alfred Mudonhi was born in Zimbabwe, and he received the B.Sc. degree in Electrical engineering from the University of Science and Technology Houari Boumediene (USTHB), Algiers, Algeria, in July 2015. He received the Master's degree in Telecommunications from the University of Trento, Trento, Italy, in March 2018 and the Ph.D. degree in Engineering Sciences and Technology from the Université catholique de Louvain (UCLouvain), Ottignies-Louvain-la-Neuve, Belgium, in May 2022. From January 2019 to January 2022, he was a PhD candidate with CEA-LETI, Grenoble, France, where he carried out his research work in Millimeter-wave massive MIMO channel characterization and modelling for 5G and 6G applications. Dr. Mudonhi's research interests include massive MIMO, wireless channel measurements and modelling, millimeter-wave propagation and modelling, channel parameter estimation, antenna characterization and Internet of Things.

Raffaele D'Errico (Senior Member, IEEE) received the Laurea degree in telecommunications engineering from the University of Bologna, Italy, in 2005, and the Ph.D. degree in physics from the University of Orsay, Paris, France, and in electronics, information, and telecommunication engineering from the University of Bologna. Since 2008, he has been a Senior Scientist and Project Manager at the CEA-LETI Grenoble, France. His research interests include radio channel sounding and modeling, antenna design and characterization, mm-wave technologies, body area networks (BANs), UWB and UHF RFID, localization, cooperative communication protocols, OTA tests, and radar. Dr. D'Errico was a French Delegate Member of the IRACON action on 5G and beyond communications. He received three Best Paper Awards, including the IEEE PIMRC 2009, IFIP NTMS 2011, and LAPC 2012 Best Student Paper. He participated to COST actions 2100 and IC1004, where he served as the Chair of the Working Group on "Body Environment."

Claude Oestges (Fellow, IEEE) received the M.Sc. and Ph.D. degrees in electrical engineering from the Université catholique de Louvain (UCLouvain), Leuven-la-Neuve, Belgium, in 1996 and 2000, respectively.In January 2001, he joined as a Post-Doctoral Scholar with the Smart Antennas Research Group (Information Systems Laboratory), Stanford University, CA, USA. From January 2002 to September 2005, he was associated with the Microwave Laboratory UCLouvain as a Post-Doctoral Fellow with the Belgian Fonds de la Recherche Scientifique (FRS-FNRS). He is currently a Full Professor with the Electrical Engineering Department, Institute for Information and Communication Technologies, Electronics and Applied Mathematics (ICTEAM), UCLouvain. He chaired the COST Action CA15104 IRACON from 2016 to 2020. He is the author or coauthor of three books and more than 200 journal papers and conference communications. Dr. Oestges was the recipient of the 1999–2000 IET Marconi Premium Award and of the IEEE Vehicular Technology Society Neal Shepherd Award in 2004 and 2012.